Results in Physics 14 (2019) 102468

Contents lists available at ScienceDirect

Results in Physics

journal homepage: www.elsevier.com/locate/rinp

Electrical and dielectric properties of Nb^{3+} ions substituted Ba-hexaferrites

M.A. Almessiere[a,b], B. Unal[c], Y. Slimani[a,*], A. Demir Korkmaz[d], N.A. Algarou[a,b], A. Baykal[e]

[a] Department of Biophysics, Institute for Research and Medical Consultations (IRMC), Imam Abdulrahman Bin Faisal University, P.O. Box 1982, 31441 Dammam, Saudi Arabia
[b] Department of Physics, College of Science, Imam Abdulrahman Bin Faisal University, P.O. Box 1982, 31441 Dammam, Saudi Arabia
[c] Department of Software and Computer Engineering, Istanbul Sabahattin Zaim University, Halkali Cad. No: 2, Halkali, Kucukcekmece, 34303 Istanbul, Turkey
[d] Department of Chemistry, Istanbul Medeniyet University, 34700 Uskudar, Istanbul, Turkey
[e] Department of Nano-Medicine Research, Institute for Research and Medical Consultations (IRMC), Imam Abdulrahman Bin Faisal University, P.O. Box 1982, 31441 Dammam, Saudi Arabia

ARTICLE INFO

Keywords:
Barium hexaferrite
Structure
Electrical conductivity
Dielectric properties

ABSTRACT

Single phase of $BaFe_{12-x}Nb_xO_{19}$ ($x \leq 0.1$) hexaferrites (HFs) were fabricated via citrate sol-gel route. The Ba hexaferrite formation has been confirmed by XRD and FE-SEM. The conductivity and dielectric properties of some Nb^{3+} ions-substituted $BaFe_{12}O_{19}$ hexaferrites (Ba-HFs) were studied extensively via impedance spectroscopy. Some important parameters; dielectric constant, conductivity, dielectric loss, complex modulus and dissipation factors were analysed at temperatures up to 120 °C in 1.0 Hz to 3.0 MHz in frequency interval for various Nb substituents. Frequency dependent conductivity was found to be in accordance with the power laws with various exponents in all frequencies studied here. Such variation can be attributed to a characteristic conduction mechanism based on tunnelling processes. Furthermore, it is clear that the contribution of the dielectric response to the dielectric parameters between grains and grain boundaries can be interpreted in a certain frequency range.

Introduction

Recently, ferrite materials exhibit unique properties such as magnetic, optical, electrical, etc, which are depends on the doping concentrations and cations occupancy in the respective sites [1–3]. Among them, M-type hexagonal ferrites (M = Sr, Ba, or Pb), which are hard magnets, have been discovered in 1950s in Philips Laboratories. Both Sr- and Ba-hexaferrite have magneto plumbite structure with a formula $MFe_{12}O_{19}$. The direction of magnetization in these uniaxial hexaferrites is along the *c*-axis. They carry out a high coercivity (H_c), saturation magnetism (M_s), magnetocrystalline anisotropy and are thermally stable above Curie temperature and have low dielectric losses [4]. Barium hexaferrites (Ba-HFs) have a wide range of electronic and technological applications including magnetic recording, microwave devices, permanent magnets, etc. [5]. Their lower prices combined with high magnetic properties have kept especially Ba-HFs highly popular.

The high electrical resistivity and low eddy current loss hexaferrites make them superior when compared to other magnetic materials [6]. Hence, ferrites should possess high resistivity as well as permittivity with a permeability for high frequency applications. The imaginary and real parts of the complex permittivity can be applied to compute dielectric loss and resonance [7]. Therefore, these properties can be altered by the substitution of different ions into the structure [8–17]. Several groups have published reports on the substitution of M-type hexaferrites with cations. For example, Ashiq et al. have prepared $SrZr_xCd_xFe_{12-2x}O_{19}$ (for $x = 0.0–0.6$) nanoparticles and found the coercivity decreased while the saturation magnetization increased with the Zr–Cd substitution [3]. Pereira and co-workers synthesized $Ba_xSr_{1-x}Fe_{12}O_{19}$ and obtained high ε' with low loss in range for radio-frequency [18]. Iqbal et al. [19] have investigated the electrical properties of $Sr_{0.5}Ba_{0.5x}Ce_xFe_{12y}Ni_yO_{19}$ ($x = 0.00–0.10$; $y = 0.00–1.00$) hexaferrites. They found out that the resistivity of the Sr-Ba-M hexaferrite increased 100-fold by substitution Ce–Ni with the increase of dielectric loss and frequency, and tangent dielectric constant decreased. V.A. Rane et al. [20] synthesized polycrystalline M-type barium hexaferrite ($BaFe_{12}O_{19}$) samples by solution combustion route at different pH and calcination conditions in order to reduce the coercivity for microwave applications in low-temperature cofired ceramic (LTCC) substrates. The VSM results show a lower coercivity (1350–3500 Oe) together with reasonably high saturation magnetization (55–60 emu/g) and a high bulk resistivity ($> 10^9$ Ω-cm) at room temperature. The bulk resistivity in excess of 10^9 Ω-cm shown by these samples would result in

* Corresponding author.
E-mail address: yaslimani@iau.edu.sa (Y. Slimani).

https://doi.org/10.1016/j.rinp.2019.102468
Received 28 May 2019; Received in revised form 20 June 2019; Accepted 20 June 2019
Available online 22 June 2019

dielectric losses low enough to meet the requirements of microwave applications in LTCC. Co–Zr doped $BaCo_xZr_xFe_{(12-2x)}O_{19}$ were prepared under sol–gel and citrate precursor sol–gel conditions [21,22]. The authors showed that by applying a suitable preparatory route Ba-hexaferrites can be easily modulated to generate materials with desired properties for specific applications. By comparing the structural and magnetic properties of prepared samples through sol–gel and citrate precursor sol–gel methods, it is observed that the substitution patterns of dopant ions on the five sublattices are quite different. This difference is clearly reflected in the M_S and H_C magnitudes. Samples prepared by sol-gel show a sharp fall in coercivity from 5428 Oe (x = 0) to 630.2 Oe (x = 1.0) than samples prepared by citrate precursor sol–gel (from 2790 Oe for x = 0 to 1210 Oe for x = 1.0). M_S varies from 63.63 to 56.94 emu/g and 62.79–53.78 emu/g in samples prepared by sol–gel and citrate precursor sol–gel methods, respectively.

There were also some studies where Nb was substituted in M-type hexaferrites in varying amounts. Fang and co-workers [23] studied the magnetic influence of doping SrM nanoparticles with zinc and niobium $Sr(Zn_{0.7}Nb_{0.3})_xFe_{12-x}O_{19}$ (x = 0–1.0). They determined the incorporation of zinc and niobium ions for iron ion increased the thermal stability while the M_s increased from 67 to 74 emu/g and the H_c decreased from 6.7 to 2.3 kOe. The effects of Nb^{3+} ions substitution on the structural, morphological, spectral and magnetic properties of $SrFe_{12}O_{19}$ hexaferrites prepared by sol-gel method were investigated [24]. The Bohr magneton number (n_B), saturation (M_s) and remanent (M_r) magnetization values increase slightly with increasing Nb^{3+} content. The obtained magnetic results were investigated deeply with relation to structural and microstructural properties. The observed remanent magnetization (M_r) and coercivity (H_c) render the products are useful for permanent magnets and high-density recording media. In another report, Zn and Nb were incorporated as $BaFe_{12-2x}Zn_xNb_xO_{19}$ in Ba M-type HFs [25]. The M_s values increased along with increasing amount of x although H_c values initially decreased and then increased. Lastly, our group have investigated the Nb incorporation on the magnetic properties of Ba M-type hexaferrites [26]. As the amount of Nb increased, the M_s, M_r, n_B and K_{eff} were initially reduced for the lowest content of Nb (x = 0.02) but increased as the "x" became higher.

All these reports mentioned above focused mainly on the magnetic properties of the doped hexaferrites. To our knowledge, the Nb substitution effects on the dielectric behavior of BaM hexaferrites have not been investigated. Thus, in this work, we have produced Nb^{3+} ion incorporated Ba M-type hexaferrites with a formula $BaNb_xFe_{12-x}O_{19}$ (x ≤ 0.1) by citrate sol-gel route.

Experimental

Sol-gel auto-combustion technique was utilized to fabrication the $BaFe_{12-x}Nb_xO_{19}$ (x ≤ 0.1) HFs. Mixtures of Iron (III) Nitrate hexahydrate ($Fe(NO_3)_3{\cdot}6H_2O$), Barium Nitrate ($BaNO_3)_2$, Niobium Chloride ($NbCl_3$) and citric acid were dissolved in DI H_2O. The solution would be sat under continue stirring for 30 min at 95 °C. Future, the pH is regulated at 7 then maintain the temperature on 150 °C for 30 min, after that raised the temperature to 330 °C. Finally, the solution will vaporize and turned to an igniting mass that release gas and then burn to the powder precursor. The powder is annealed at 1100 °C for 5 h to get the pure Ba hexaferrite phase. The phase of Nb substituted Ba hexaferrite was verified by Rigaku Benchtop Miniflex powder X-ray diffraction (XRD) analyzer with CuKα radiation. The surface analysis was proceeded through field emission scanning electron microscope (FE-SEM) (FEI Titan S/TEM) coupled with energy-dispersive X-ray spectroscopy (EDX). The conductivity and dielectric measurements done by Novocontrol Alpha-N high-resolution dielectric-impedance analyzer.

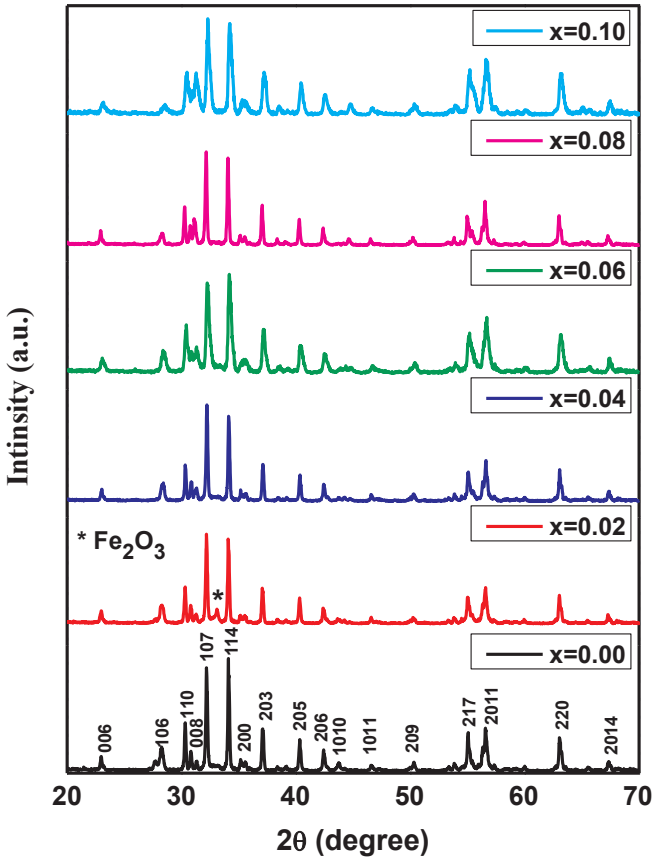

Fig. 1. XRD patterns for $BaFe_{12-x}Nb_xO_{19}$ (x ≤ 0.1) HFs.

Results and discussion

Structure and surface analyses

$BaFe_{12-x}Nb_xO_{19}$ (x ≤ 0.1) HFs phase identification was shown in Fig. 1. The XRD powder patterns indicated that the indexed peaks correspond to the pure phase of Ba hexaferrite, excepting a minor impurity of Fe_2O_3 is presented at x = 0.02. The Rietveld refined structural parameters are listed in Table 1. It is found that the lattice parameters increased with increasing Nb ions content, which is principally due to the substitution of Fe^{3+} having ionic radii of 0.64 Å by Nb ions having larger ionic radii (0.69 Å) [26]. Details of XRD analysis has been already presented in our recent study [26]. Fig. 2 illustrated the FE-SEM images of $BaFe_{12-x}Nb_xO_{19}$ (x ≤ 0.1) HFs. All ratios revealed a uniform distribution of particles with hexagonal structure. The particles are tended to aggregation caused by magnetic interaction between particles [27–30]. It is noticed that the particles size decreased slightly with increasing the Nb content. EDX and elemental mapping analyses proved the formation of the required stoichiometries that have been used for preparing samples as seen in Fig. 3.

Table 1
Structural parameters for $BaFe_{12-x}Nb_xO_{19}$ (x ≤ 0.1) HFs.

x	a = b (Å)	c (Å)	V(Å^3)	D_{XRD} (nm)
0.00	5.891	23.1870	696.948	46.1
0.02	5.891	23.1973	696.962	46.0
0.04	5.894	23.1979	697.666	43.5
0.06	5.894	23.1980	697.704	41.6
0.08	5.897	23.2100	698.224	36.0
0.10	5.897	23.2317	699.698	33.2

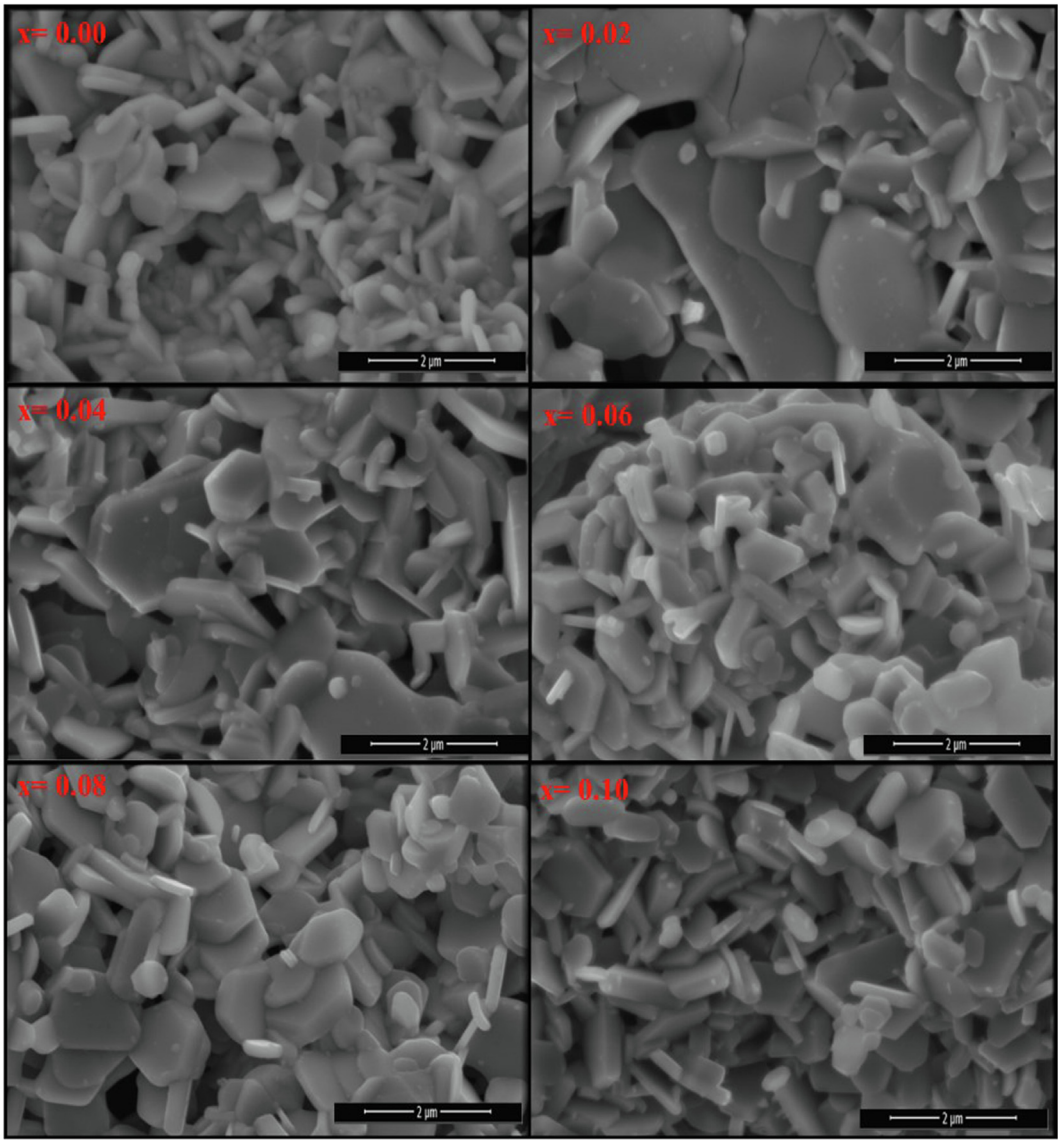

Fig. 2. FE-SEM images of $BaFe_{12-x}Nb_xO_{19}$ ($x \leq 0.1$) HFs.

Impedance spectroscopy

Impedance spectroscopy is used to study the electrical properties of doped and non-doped M-type hexaferrites such as conduction mechanisms, dielectric properties under the variation of frequencies and temperatures as well as substitution levels. The conductivity of the M type hexaferrites was evaluated by using an impedance analyser at frequency interval of 1 Hz up to 3 MHz with an *ac* electric field of about 1.0 V/cm. The *ac*-conductivity has been determined from the real component of the measured impedance by a standard relation together with the correction electrode and sample geometrical factors. For the evaluation purposes, the admittance of the measured samples is equal to [31]:

$$Y(\omega; T; x) = G + i\omega C = i\omega\left(\frac{C}{C_0} - i\frac{G}{\omega C_0}\right)C_0 \quad (1)$$

where C_0 and C are the *air–filled*, and *material-filled* capacitance across the parallel plates, respectively. G = 1/R. So, complex relative permittivity for the temperature- and substitution-dependent hexaferrites is defined as [31,32]:

$$\varepsilon^*(\omega; T; x) = \varepsilon_r'(\omega; T; x) - i\varepsilon_r''(\omega; T; x) \quad (2)$$

The complex conductivity is expressed by [32]:

$$\sigma^*(\omega; T; x) = \sigma'(\omega; T; x) - i\sigma''(\omega; T; x) \quad (3)$$

The dielectric constant (ε_r') and dielectric loss (ε_r''), dielectric loss tangent (tan δ) is determined using the customary equations as follows [32]:

$$\varepsilon_r'(\omega; T; x) = \frac{C(\omega; T; x)d}{\varepsilon_0 A} \quad (4)$$

$$\varepsilon_r''(\omega; T; x) = \frac{G(\omega; T; x)d}{\omega\varepsilon_0 A} = \varepsilon_r'(\omega; T; x)tan\delta \quad (5)$$

where A is cross-sectional surface area of the pellet in m^2 and d is the gap across double-coupled electrode, and ε_0 is the vacuum dielectric permittivity of 8.852×10^{-12} F/m). It is clear to see that the *ac*-conductivity (σ_{ac}) is derived from the dielectric loss in relation to equation of [32]:

$$\sigma_{ac}(\omega; T; x) = \omega\varepsilon_0\varepsilon_r''(\omega; T; x) = \omega\varepsilon_0\varepsilon_r'(\omega; T; x)tan\delta \quad (6)$$

The electrical characterization of any submicron-sized samples shows some key mechanisms based on the substitutional dopant(s) of any relevant elements and their distributions in host hexaferrites. So,

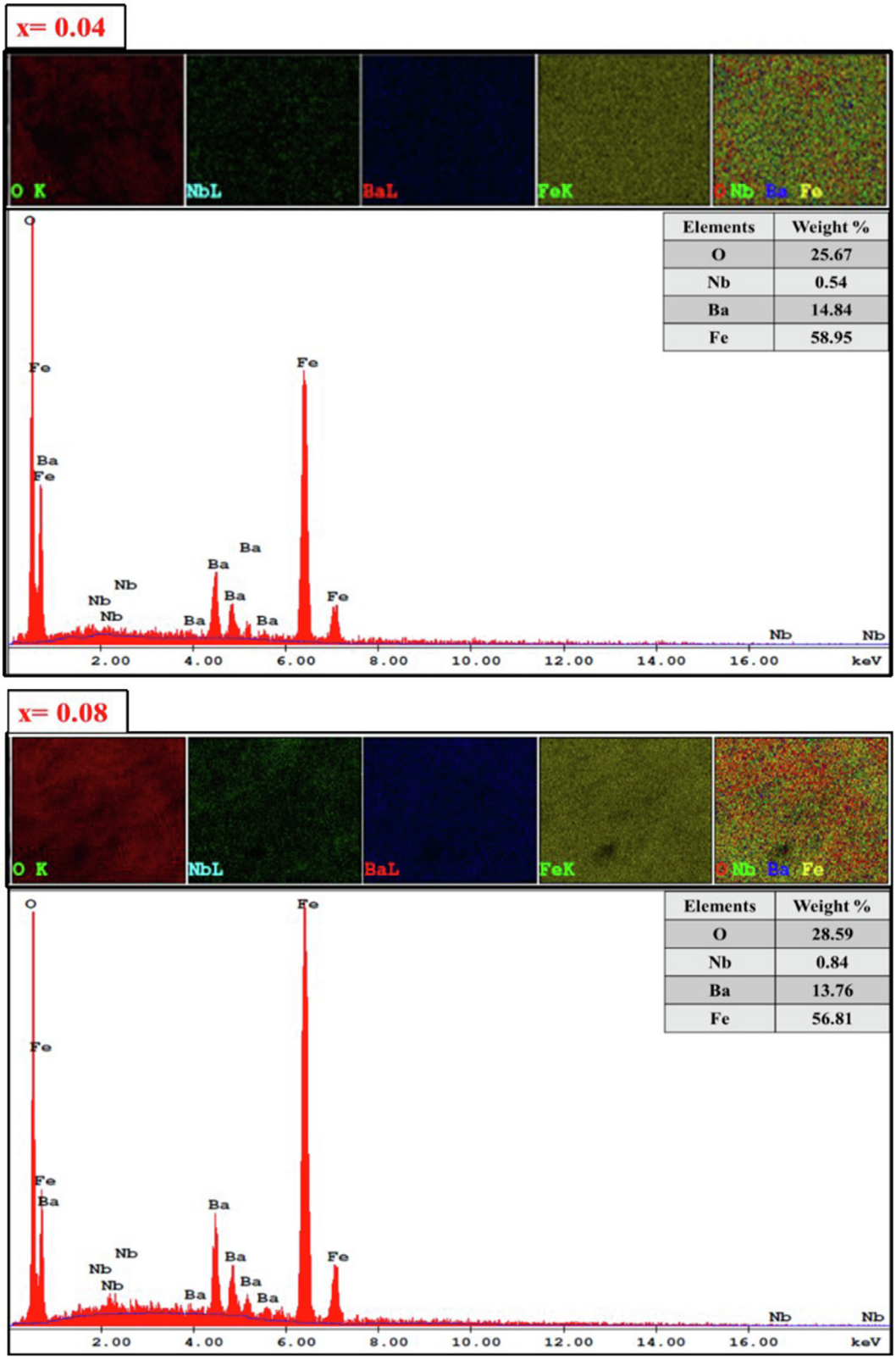

Fig. 3. EDX and elemental mapping of $BaFe_{12-x}Nb_xO_{19}$ (x = 0.04 and 0.08) HFs.

the conduction mechanism can be divided into two components that are notable for certain substituents in hexaferrites: These are assigned to ac-conductivity due to the *hopping mechanism* between ions of the same element occurring in multiple valence states and dc-conductivity attributable to *band conduction*. From a theoretical interpretation, the *ac/dc* conductivity, dielectric constant, dielectric loss as well as dissipation factor are examined as functions of frequency, temperature and the substituent level, utilizing an impedance analyser in the frequency range up to 3.0 MHz and temperatures up to 120 °C, and also a variety of substitutional ratios up to *0.08* including non-substituent

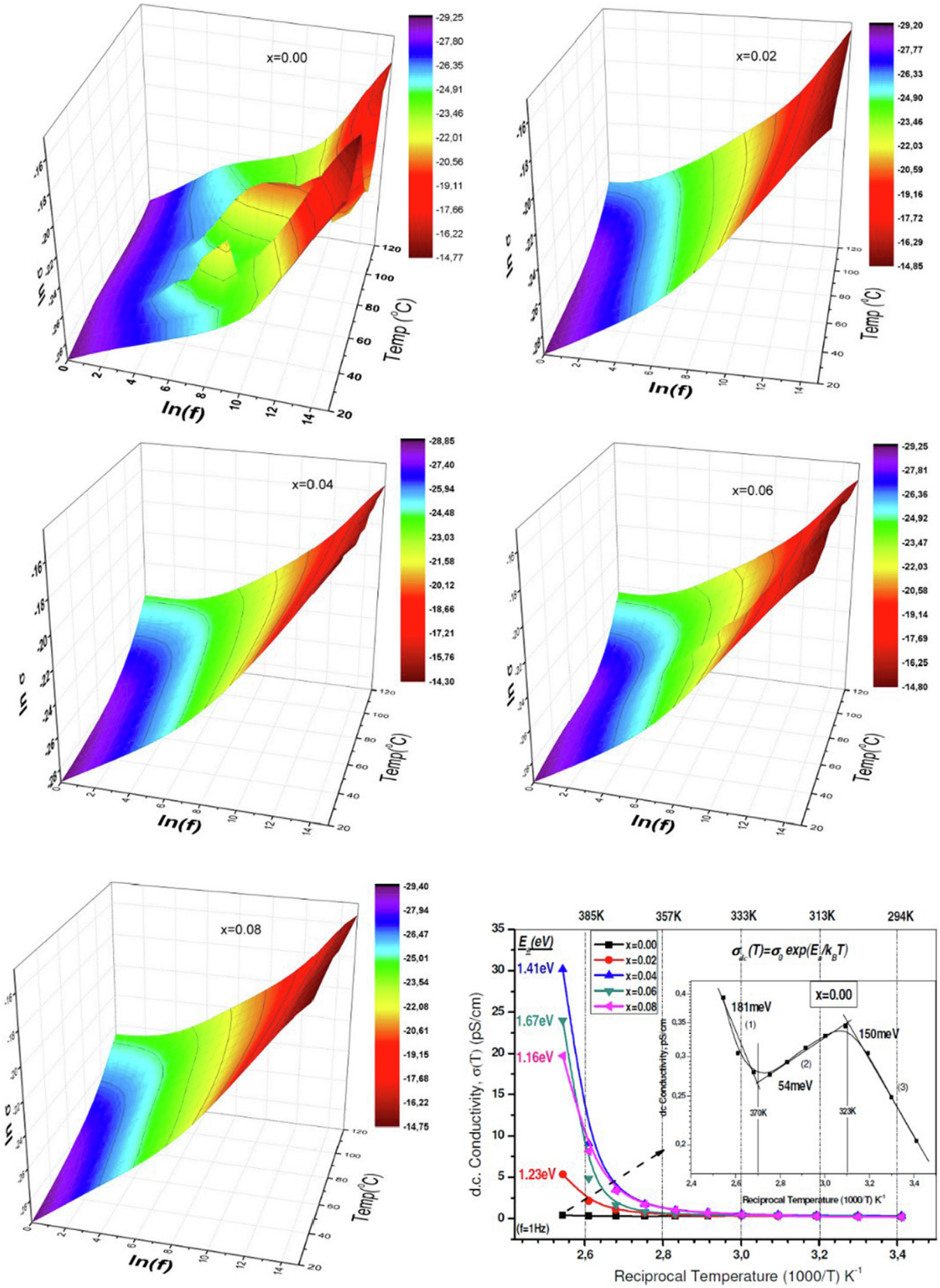

Fig. 4. 3D characteristic representations of *ac* conductivity of $BaNb_xFe_{12-x}O_{19}$ ($x \leq 0.08$) HFs as functions of frequency up to 3 MHz, and for temperatures up to 120 °C. Last graph shows dc conductivity as a function of reciprocal temperature for some substitutional Nb ion ratios.

hexaferrites.

ac conductivity

The ac-conductivity measurements of Nb ion substituted M-type barium hexaferrites were carried out as a function of both frequency and temperature from a well-known technique of impedance spectroscopy. The 3D plots of conductivity of $BaNb_xFe_{12-x}O_{19}$ HFs for a variety of substitutional ratios x is shown in Fig. 4 as functions of frequency up to 3 MHz, and for temperatures up to 120 °C from RT. Hence, the frequency-dependent complex conductivity of all the hexaferrites can be calculated from the following standard equation [32–34]:

$$\sigma'(\omega; T; x) = \sigma_{ac}(\omega; T; x) = \varepsilon''(\omega; T; x)\omega\varepsilon_0 \quad (7)$$

where *σ'(ω, T, x)* is the real component of conductivity, ω is the angular frequency of *ac* signal potential of 1.0 V_{pp} applied across the coupled parallel plate electrodes.

Therefore, it is well-known that the frequency-dependent variation of conductivity for a variety of both temperature and substitutional ratios gives us some substantial evidence to understand the conduction mechanism. It is clear to understand that *ac*-conductivity for Nb ion substituted Ba-hexaferrites ($0.0 \leq x \leq 0.08$) changes significantly with a frequency ranging up to 3 MHz while some imperative effect could be observed by means of temperature-correlated activation in the conduction mechanisms between RT and 120 °C.

When Ba-HFs is compared with a Nb ion substituted ones, it is observed that ac-conductivity of Ba-HFs obeys the rule of power law at certain temperature however, Nb-substituted ones is consistent with the frequency dependent power law for all temperature. It is necessary to note that substituted one with x = 0.06 give us some mid-temperature related variations at about 60 °C. It can be clearly seen from Fig. 4 that two temperature-relevant humps at about 60 °C and 90 °C is observed in the graphs of x = 0.00 while one relevant hump is shown in the graph of x = 0.06. It can be considered that frequency relevant power law dependence at lower temperature is more consistent than higher ones and also it can be expressed that level of Nb ion substitution regulates the conduction mechanism of Ba-HFs.

dc conductivity

The *dc*-conductivities (σ_{dc}) of Nb-substituted Ba-HFs were extracted from the well-established plateau region in *3D* plots of natural $log\sigma_{ac}$ versus *logf* by a linear fitting at a frequency of 1.0 Hz. The *dc*-conductivity as a function of reciprocal temperature are evaluated for each of the whole Ba-HFs ($0.00 \leq x \leq 0.08$). Consequently, *dc*-conductivity can be formulated from a well-known Arrhenius plot for some substitutional *Nb* ion ratios. The linearity in *dc*-conductivity from the Arrhenius plot in Fig. 4 changes slightly with the substitutional ratio. It has been indicated that the conductivity of Nb^{3+} ion substituted Ba-HFs is thermally activated and conduction mechanism can be elucidated from the following Arrhenius relation [34]:

$$\sigma_{dc}(T; x) = \sigma(0; x)\exp\left[-\frac{E_a(x)}{k_B T}\right] \quad (8)$$

where σ_{dc} stands for dc conductivity for a variety of substituent level, *σ(0,x)* is the pre-exponential term for each substituted ferrites, E_a is the substitution dependent activation energy, k_B is the Boltzmann constant (8.617×10^{-5} eV·K^{-1}) and T is the temperature in K. Activation energy may displays some variation by changing the substitutional ratios of Nb^{3+} ions. This can be attributable to more energy required for active charge carriers to hop from one cationic site to another by increasing the number of both *doping* ions. So, resulting tendencies may cause an increase in activation energies for all substituted ferrites except for x = 0.08. Subsequently, incremental tendencies in *dc*-conductivity with temperature reveal that the Nb^{3+} ion-substituted Ba-HFs lead to a semiconductor-like behavior in some extent.

Furthermore, when a small amount of substitutional Nb^{3+} ions is added up in the host Ba-hexaferrites, dc-conductivity at 120 °C rises up to a value of 5 pS/cm for x = 0.02; 19 pS/cm for x = 0.08; 24 pS/cm for x = 0.06 and finally 30 pS/cm for x = 0.04, attributable to the energetic hopping conduction mechanism among the ferric and ferrous ion centers as shown in 2D graph of Fig. 4. For non-substituted M-type Ba-hexaferrites the temperature dependency of *dc*-conductivity represents three activation region such as 150 meV for low temperature region; 54 meV for medium temperature region and 181 meV for high temperature region for the elevated temperatures up to 120 °C while other substituted ferrites gives us a single activation energy such as 1.23 eV for x = 0.02; 1.41 eV for x = 0.04; 1.67 eV for x = 0.06; 1.16 eV for x = 0.08. In this case, it is stated that electrical conduction is caused by both electron and polaron hopping mechanism. In another word, the activation energy of Ba-hexaferrites is found to be less than 0.4 eV at all temperatures, which indicates that conduction might be only due to *small polaron hopping* mechanisms. Additionally, the activation energy of Nb-substituted Ba-hexaferrites is calculated to be higher than 1.0 eV at all temperatures, which tells us that the conduction might be just due to *electron hopping* mechanisms, which is differing from that of a variety of substituted spinel ferrites [35].

Dielectric constant

3D representation of the dielectric constant of Nb-substituted Ba-HFs ($0.0 \leq x \leq 0.08$) as a function of frequency up to 3 MHz is depicted in Fig. 5 for temperature range up to 120 °C with an interval of 10 °C. It can be seen that dielectric constants of Nb-substituted Ba-HFs have some similarities in tendencies along temperatures up to 120 °C while Ba-HFs sample shows a completely different trend along temperature variation, say, first a plateau occurred at lower frequency for all temperature ranges, and a deep valley observed around 70 °C, especially for medium and high frequency regions.

It is also note that dielectric constant of Ba-HFs at low frequency varies between 1.22 and 1.82 at some elevated temperatures up to 120 °C while that of Nb-substituted Ba-HFs, once again, at low frequency gives us some incremental values of 1.82–3.32 for x = 0.02; 2.23–3.32 for x = 0.04; 1.82–4.06 for x = 0.06 and 2.72–5.21 for x = 0.08 at the elevated temperature varying from 20 °C to 120 °C. Therefore, the substitution of Nb ion to Ba-HFs causes an increase in the dielectric constant of ferrites. Dielectric constant reduces with the increase of frequency for substituted Ba-HFs while the one for Ba-HFs first decreases, and then kept almost constant, except for a deep valley in mid-temperature region. A comparable tendency can also be seen clearly for *ac*-conductivity curves for similar substitutions. The space charge polarization appears to be attributable to electron displacement when electric field is applied across Nb-substituted Ba-HFs sample.

Dielectric loss

3D characteristic representations of the dielectric loss of substituted Ba-HFs for a variety of substitution ratios of ($0.00 \leq x \leq 0.08$) are shown in Fig. 6 as functions of frequency up to 3 MHz for temperature up to 120 °C from RT. Generally, it is seen that the dielectric loss in Ba-HFs substituted with many Nb^{3+} ions shows both frequency and temperature dependence, a decrease in low frequency regime, and a minimum value in mid-frequency region and a steady increase in high-frequency region. For Ba-HFs sample, dielectric loss reaches a minimum at mid frequency region while it fluctuates with the elevated temperature in higher frequency range. For other Nb-substituted Ba-HFs samples, the variation trend in loss curves is regulated with the substituent levels in some manner, the minimized valley located at mid-frequency is shifted to, and narrowed in higher frequency side. So, this case is more significant at lower frequencies, similarly, all curves show a common trend at high frequencies, which slightly changes with

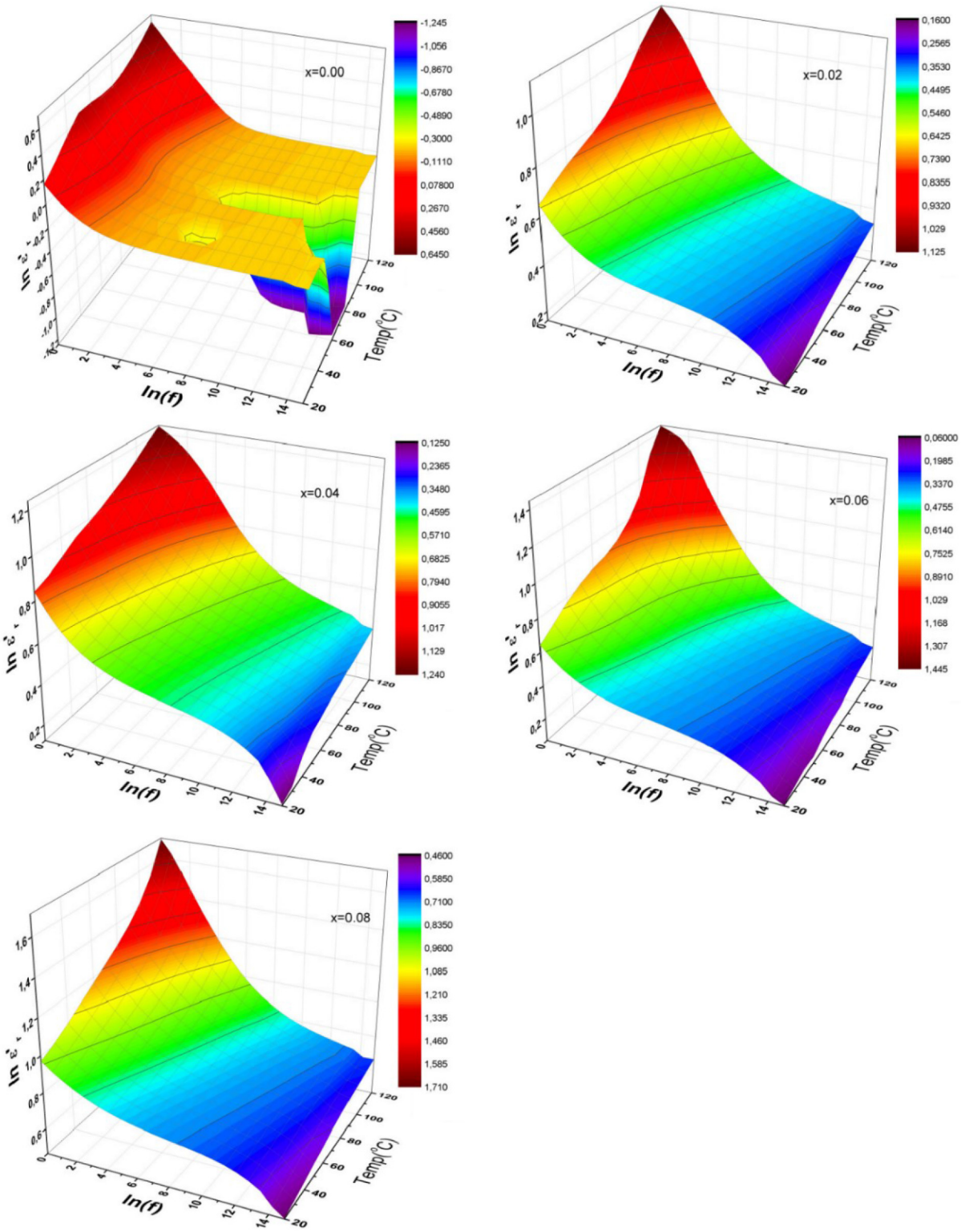

Fig. 5. 3D characteristic representations of dielectric constant of $BaNb_xFe_{12-x}O_{19}$ ($x \leq 0.08$) HFs as a function of frequency up to 3 MHz, and for temperatures up to 120 °C.

substituting Nb^{3+} ion ratios. In low frequency region this linearity behavior in natural log-log plot can be expressed with *dc*-conductivity as [33,34]:

$$\varepsilon''_{dc}(\omega; T; x) = \omega C_o \sigma_{dc}(T; x) \quad (9)$$

It can be noted that conduction mechanism is associated with somehow temperature consequences as well as the reorganization process caused by some structural diffusion between elemental compositions. There could be more evident to note that the capacitive contribution leads to high temperature-dependent consistency rather than reorganizational nature of Nb^{3+} ions-substituted Ba-HFs. Therefore, any reduction in dielectric loss of Nb-substituted Ba-HFs ultimately reaches a minimum level at a given frequency depending on the level of substitution rate, and then is varied slightly with

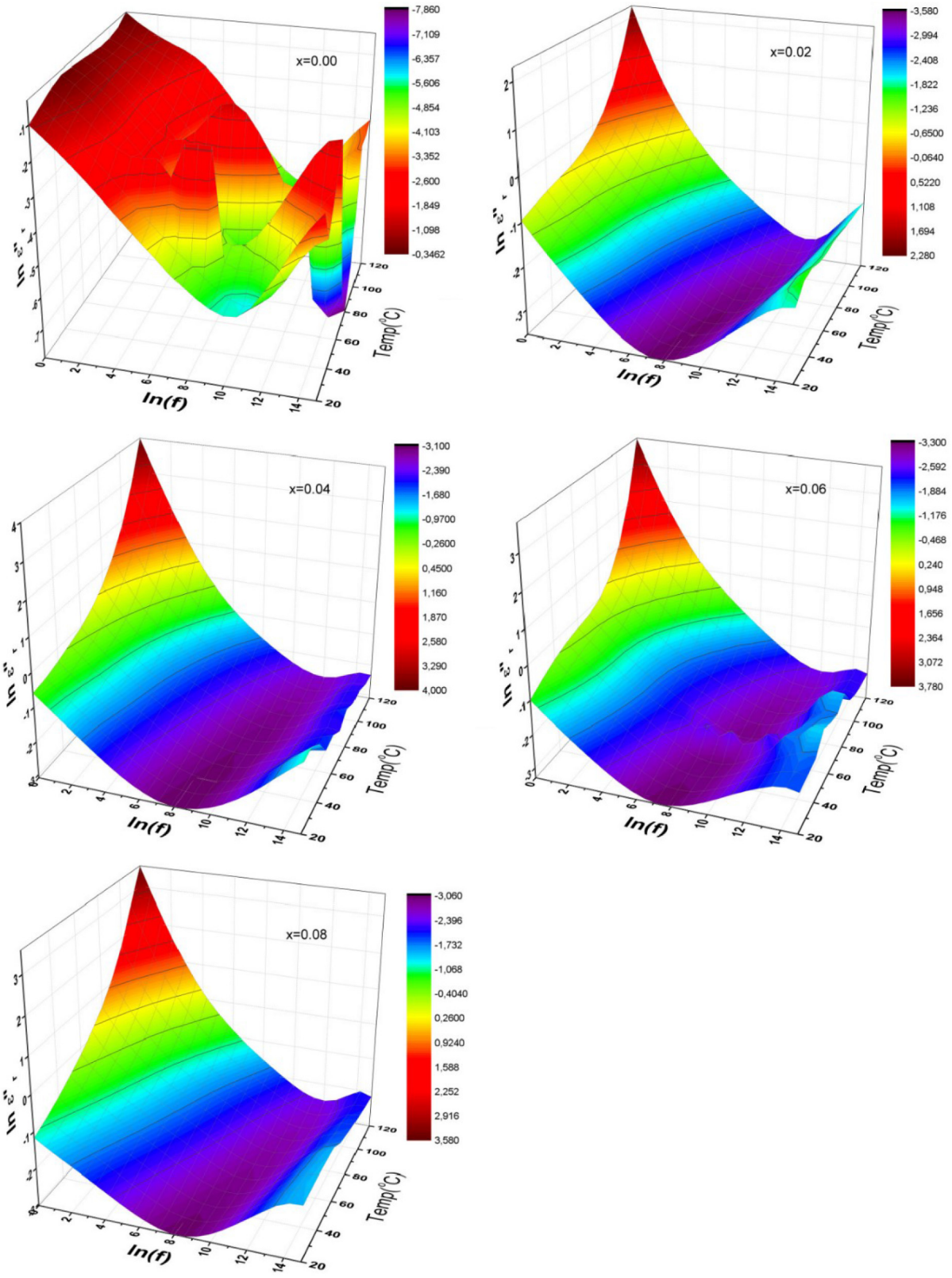

Fig. 6. 3D characteristic representations of dielectric loss of $BaNb_xFe_{12-x}O_{19}$ ($x \leq 0.08$) HFs as a function of frequency up to 3 MHz, and for temperatures up to 120 °C.

temperature along higher frequency side in dependence of substitution ratio in Ba-HFs while dielectric loss for Ba-HFs fluctuates with temperature in higher frequency range.

The magnitudes of dielectric loss measured at lowest frequency for temperatures between RT and 120 °C are found to be from 0.36 to 0.60 for x = 0.00; from 0.36 to 8.17 for x = 0.02; from 0.61 to 54.6 for x = 0.04; from 0.36 to 36.6 for x = 0.06, and from 0.33 to 30.0 for x = 0.08. This result indicates that the substitution of Nb ions in Ba-HFs

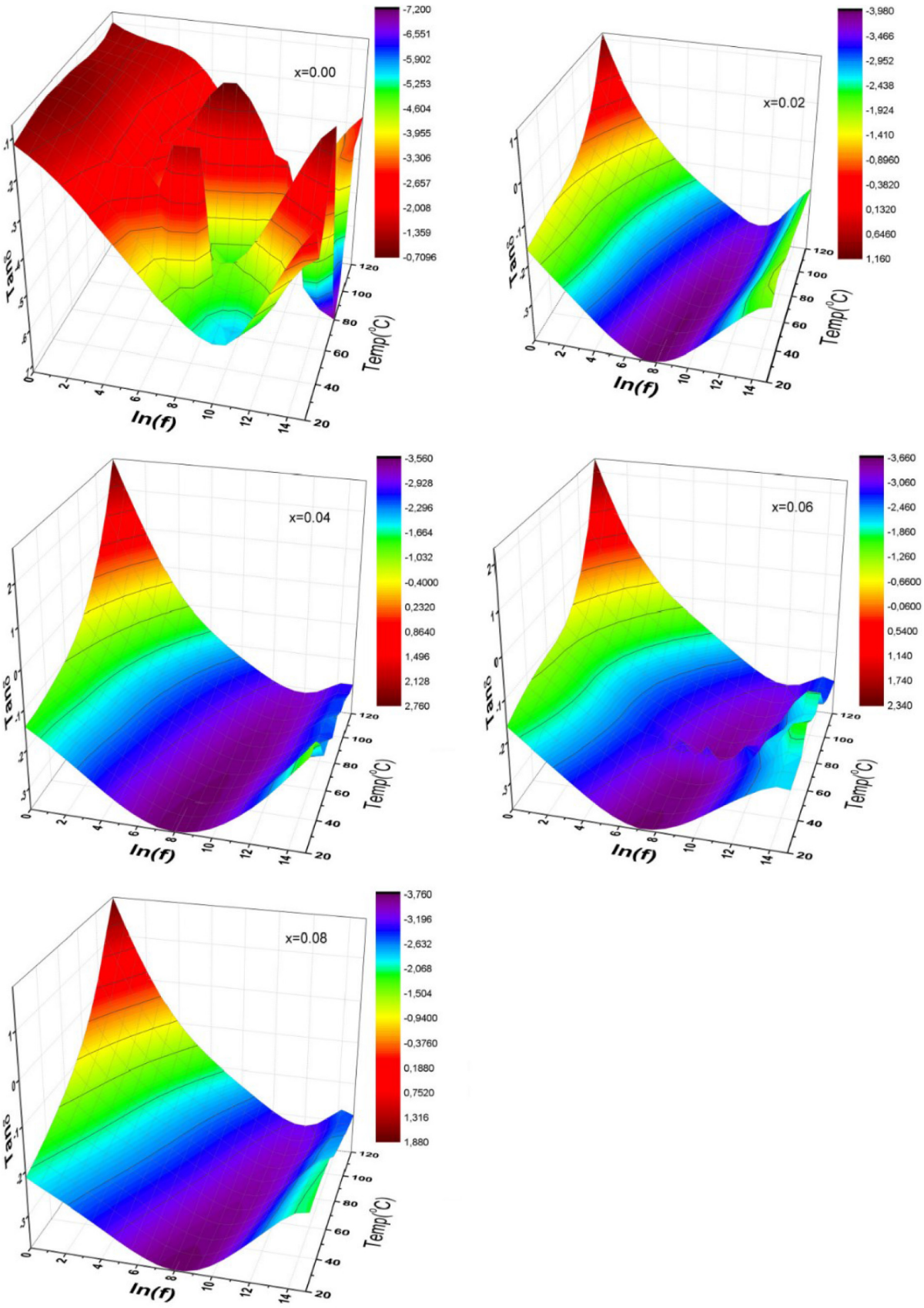

Fig. 7. 3D characteristic representations of dielectric tangent loss of $BaNb_xFe_{12-x}O_{19}$ ($x \leq 0.08$) HFs as a function of frequency up to 3 MHz, and for temperatures up to 120 °C.

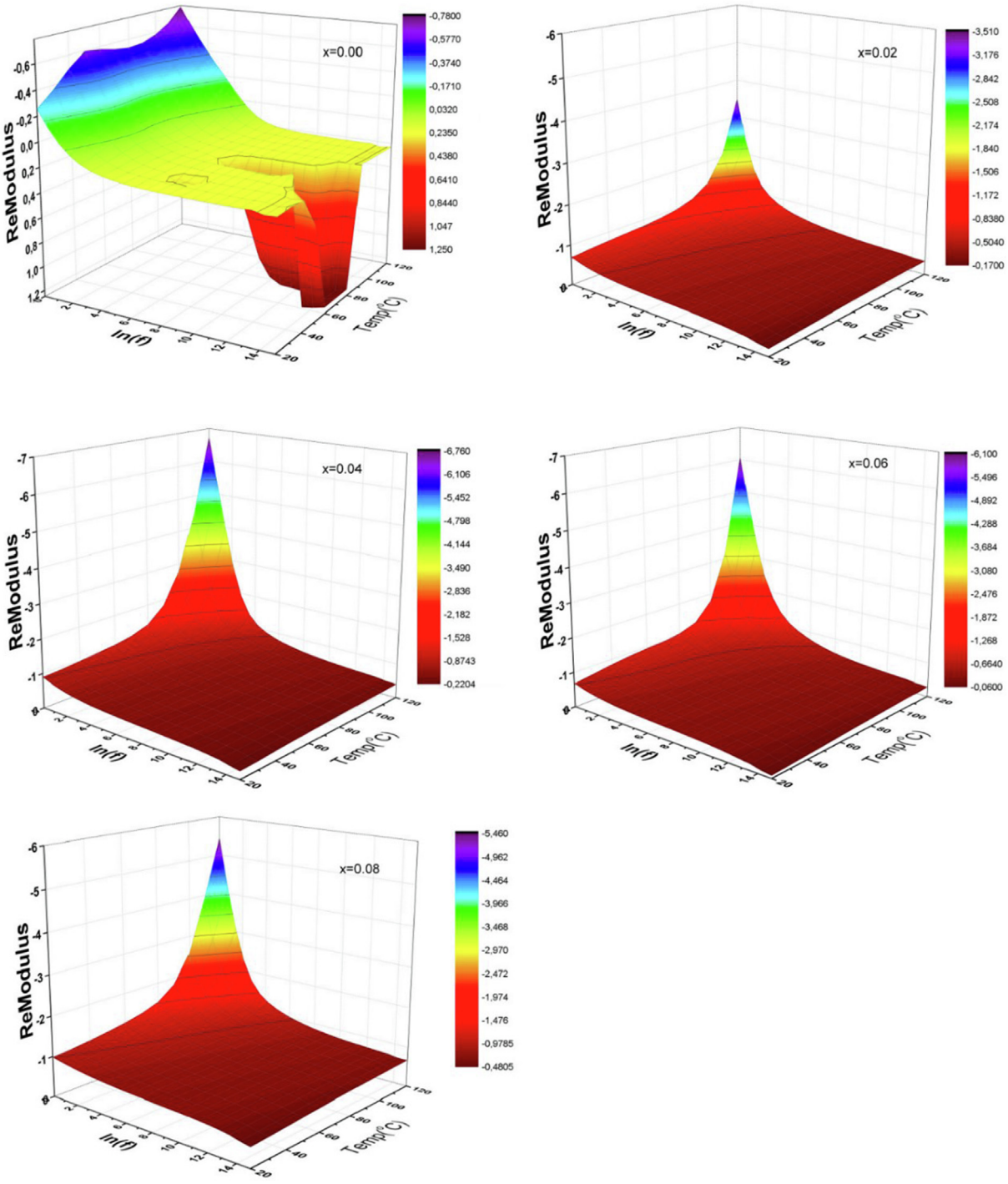

Fig. 8. 3D characteristic representations of dielectric real modulus of $BaNb_xFe_{12-x}O_{19}$ ($x \leq 0.08$) HFs as a function of frequency up to 3 MHz, and for temperatures up to 120 °C.

regulates the curve of dielectric loss, so the substitution causes a 100-fold increase in dielectric loss. Therefore, the dielectric compound (i) is composed of conductive ferrite grains having a very good structure, (ii) an electrically isolated layer with fine-grained borders. Grain boundaries occur due to the superficial reduction of micro-sized hexaferrites. It can be understood that grain boundaries are effective at low frequency with a small conductivity; ferrite grains are more effective at high frequency with greater conductivity [36]. Such trends indicate that the dielectric constant and the dielectric loss decreases with increasing frequency as the frequency increases. Therefore, the dielectric properties of any heterogeneous structure can also be explained by the Koop's theory of the Maxwell-Wagner model [37]. For these substituted samples, all these effects can be attributed to the results of the combinations of both electron and polaron hopping conduction mechanisms. As a result, this gradient in the dielectric parameters is caused by temperature, frequency and substitution as well as by barium ions in ferrite [35].

Dissipation factor

3D characteristic plot of the dissipation factors (tan δ), named as the ratio of dielectric loss to dielectric constant, of *Nb* ion- substituted Ba-

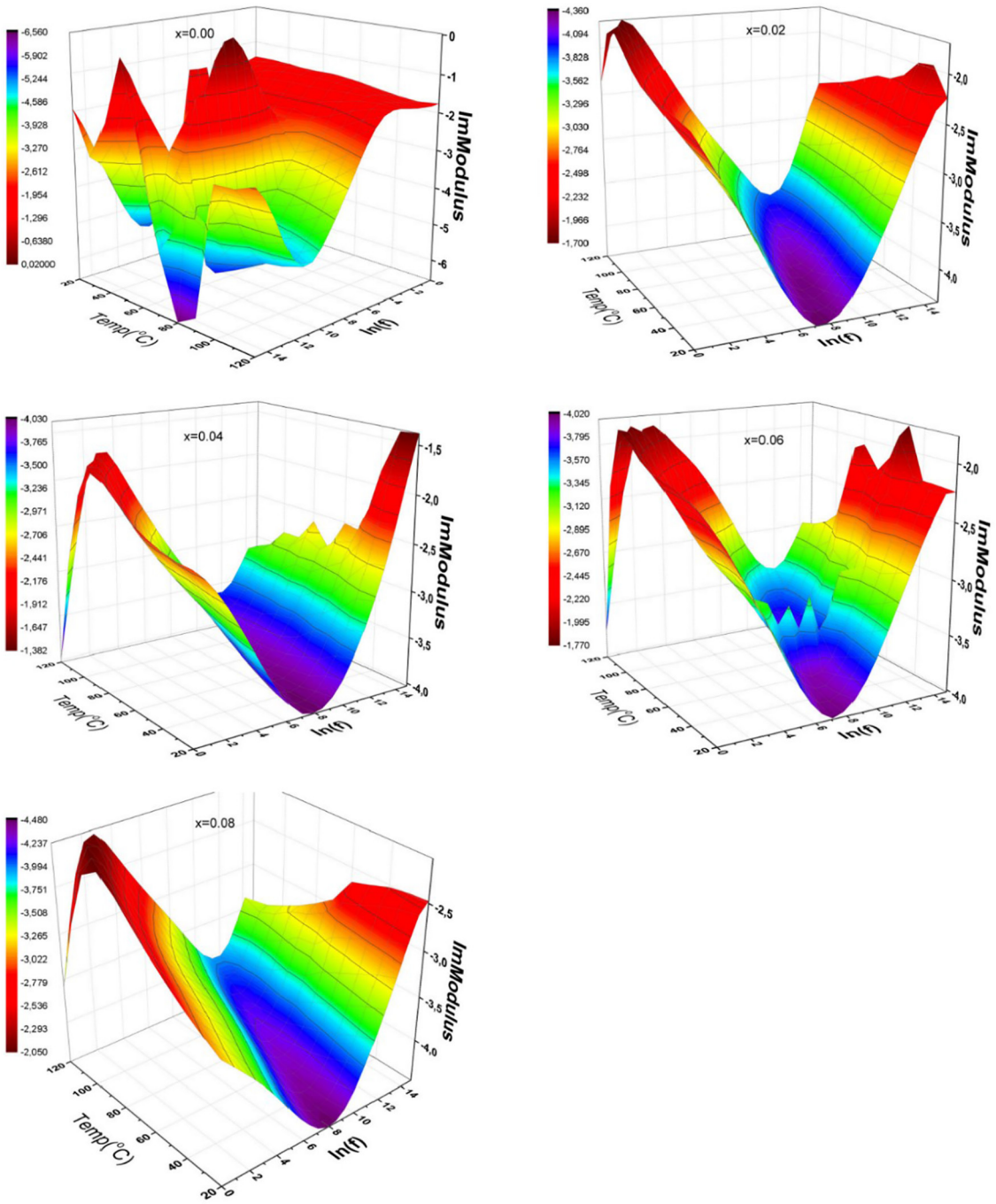

Fig. 9. 3D characteristic representations of dielectric imaginary modulus of $BaNb_xFe_{12-x}O_{19}$ ($x \leq 0.08$) HFs as a function of frequency up to 3 MHz, and for temperatures up to 120 °C.

HFs as functions of both temperature and frequency were depicted in Fig. 7 for a variety of substitutional ratios.

As it is seen from Fig. 7, the dispersion factor appears to be very little rise along temperature ranges for Ba-HFs, especially at lower frequencies. At medium and higher frequencies, it fluctuates along entire temperature ranges as reaching a minimum at mid frequency. Similar tendencies for both temperature and frequency variation of Nb-substituted Ba-HFs were observed for dissipation factors as in the case of dielectric loss. Thus, this type of variations can be attributed to *ac*-field assisted dipole orientations as discussed in the literature [6,38–40].

Dielectric modulus

3D characteristic representation of the real dielectric modulus of $BaNb_xFe_{12-x}O_{19}$ samples for substitution ratio of $0.00 \leq x \leq 0.08$ is shown in Fig. 8 as functions of frequency up to 3 MHz, and temperatures up to 120 °C. For all substitution ratios, it can be seen that each curve leads to a similar tendency for both temperature and frequency, while the Ba-HFs fluctuate by changing with frequency at high temperatures. The magnitude of the real modulus has a maximum value at low frequency for high temperatures. However, the real modulus for substituted Ba-HFs decreases for both higher temperature and higher frequencies, while those for Ba-HFs leads to a plateau with a deep valley at medium temperature for the high frequency region.

The 3D characteristic representation of the imaginary modulus for some substitution ratios is shown in Fig. 9 on the functions of the frequency up to 3 MHz and from RT to 120 °C. Ba-HFs exhibit a significantly higher fluctuation in the dielectric imaginary modulus, while a significantly different variation is shown for the substituted Ba-HFs. The imaginary modulus of the substituted samples leads to V-shaped trends, while shifting the minimum value slightly to higher frequency side in addition to a small peak at mid frequency and temperature. Consequently, the above discussion shows that the substitution process has a significant effect on the dielectric properties.

Conclusion

Nb substituted Ba hexaferrites with crystallite size in the range 33–46 nm are fabricated by citrate sol gel route. According to XRD and SEM results, the Ba hexaferrite phase and hexagonal morphology were confirmed. Electrical characterization of Nb-substituted Ba-HFs explained that *ac*-conductivity corresponds to a power base law of an exponent for entire substituent ratios. The substitution to the host Ba-HFs result in better electrical bonds stabilities, and influential reorganization formed between the substituent ions and the host ferrous ions in Ba-HFs. Similarly, the various level of the substituent, Nb, in Ba-hexaferrites provide us with a better optimization and tunability in dielectric constant, conductivity and tangent loss as well as dissipation factor.

Acknowledgement

Authors highly acknowledged the financial assistances from the Institute for Research & Medical Consultations (Projects No. 2017-IRMC-S-3, No. 2018-IRMC-S-1, and No. 2018-IRMC-S-2) and the Deanship of Scientific Research (Projects No. 2017-605-IRMC, No. 2017-576-IRMC, and No. 2018-209-IRMC) of Imam Abdulrahman Bin Faisal University (IAU – Saudi Arabia).

References

[1] Mary Jacintha A, Manikandan A, Chinnaraj K, Arul Antony S, Neeraja P. Comparative studies of spinel $MnFe_2O_4$ nanostructures: structural, morphological, optical, magnetic and catalytic properties. J Nanosci Nanotech 2015;15:9732–40.
[2] Hema E, Manikandan A, Karthika P, Durka M, Arul Antony S, Venkatraman BR. Magneto-optical properties of reusable spinel $Ni_xMg_{1-x}Fe_2O_4$ ($0.0 \leq x \leq 1.0$) nanocatalysts. J Nanosci Nanotech 2016;16:7325–36.
[3] Hema E, Manikandan A, Gayathri M, Durka M, Arul Antony S, Venkatraman BR. The role of Mn^{2+}-doping on structural, morphological, optical, magnetic and catalytic properties of spinel $ZnFe_2O_4$ nanoparticles. J Nanosci Nanotech 2016;16:5929–43.
[4] Pullar RC, Appleton SG, Bhattacharya AK. The manufacture, characterization and microwave properties of aligned M ferrite fibres. J Magn Magn Mater 1998;186(3):326–32.
[5] Mallick KK, Shepherd P, Green RJ. Dielectric properties of M-type barium hexaferrite prepared by co-precipitation. J Eur Ceram Soc 2007;27(4):2045–52.
[6] Ashiq MN, Iqbal MJ, Gul IH. Structural, magnetic and dielectric properties of Zr–Cd substituted strontium hexaferrite ($SrFe_{12}O_{19}$) nanoparticles. J Alloy Compd 2009;487:341–5.
[7] Auwal IA, Ünal B, Güngüneş H, Shirsath SE, Baykal A. Dielectric properties, cationic distribution calculation and hyperfine interactions of La^{3+} and Bi^{3+} doped strontium hexaferrites. Ceram Int 2016;42:9100–15.
[8] Yang Y, Wang F, Shao J, Huang D, He H, Trukhanov AV, et al. Influence of Nd-NbZn co-substitution on structural, spectral and magnetic properties of M-type calcium-strontium hexaferrites $Ca_{0.4}Sr_{0.6-x}Nd_xFe_{12.0-x}(Nb_{0.5}Zn0_{.5})_xO_{19}$. J Alloy Compd 2018;765:616–23.
[9] Almessiere MA, Slimani Y, Sertkol M, Nawaz M, Baykal A, Ercan I. The impact of Zr substituted Sr hexaferrite: investigation on structure, optic and magnetic properties. Results Phys 2019;13:102244.
[10] Almessiere MA, Slimani Y, Gungunes H, Manikandan A, Baykal A. Investigation of the effects of Tm^{3+} on the structural, microstructural, optical, and magnetic properties of Sr hexaferrites. Results Phys. 2019;13:102166.
[11] Trukhanov AV, Almessiere MA, Baykal A, Trukhanov SV, Slimani Y, Vinnik DA, et al. Influence of the charge ordering and quantum effects in heterovalent substituted hexaferrites on their microwave characteristics. J Alloy Compd 2019;788:1193–202.
[12] Almessiere MA, Slimani Y, Güngüneş H, Ali S, Baykal A, Ercan I. AC susceptibility and hyperfine interactions of Mg-Ca ions co-substituted $BaFe_{12}O_{19}$ nanohexaferrites. Ceram Int 2019;45:10048–55.
[13] Almessiere MA, Slimani Y, EL Sayed HS, Baykal A. Morphology and magnetic traits of strontium nanohexaferrites: effects of manganese/yttrium co-substitution. J. Rare Earths 2019;37(7):732–40.
[14] Almessiere M, Slimani Y, Güngüneş H, Baykal A, Trukhanov SV, Trukhanov AV. Manganese/yttrium co-doped strontium nanohexaferrites: evaluation of magnetic susceptibility and mossbauer spectra. Nanomaterials 2019;9:24.
[15] Almessiere MA, Slimani Y, Baykal A. Impact of Nd-Zn co-substitution on microstructure and magnetic properties of $SrFe_{12}O_{19}$ nanohexaferrite. Ceram Int 2019;45:963–9.
[16] Almessiere MA, Slimani Y, El Sayed HS, Baykal A, Ali S, Ercan I. Investigation of microstructural and magnetic properties of $BaV_xFe_{12-x}O_{19}$ nanohexaferrites. J Supercond Nov Magn 2019;32:1437–45.
[17] Almessiere MA, Slimani Y, Güngüneş H, Baykal A, Alhamed NA, Trukhanov AV, et al. Structure, mössbauer and AC susceptibility of strontium nanohexaferrites: effect of vanadium ions doping. Ceram Int 2019;45:11615–24.
[18] Pereira FMM, Junior CAR, Santos MRP, Sohn RST, Freire FNA, Sasaki JM, et al. Structural and dielectric spectroscopy studies of the M-type barium strontium hexaferrite alloys ($Ba_xSr_{1-x}Fe_{12}O_{19}$). J Mater Sci: Mater Elect 2008;19:627–38.
[19] Iqbal MJ, Farooq S. Extraordinary role of Ce–Ni elements on the electrical and magnetic properties of Sr–Ba M-type hexaferrites. Mater Res Bull 2009;44:2050–5.
[20] Rane Vivek A, Meena Sher Singh, Gokhale Suresh P, Yusuf SM, Phatak Girish J, Date Sadgopal K. Synthesis of low coercive $BaFe_{12}O_{19}$ hexaferrite for microwave applications in low-temperature cofired ceramic. J Electron Mater 2013;42:761–8.
[21] Mudsainiyan RK, Chawla SK, Meena SS. Correlation between site preference and magnetic properties of Co–Zr doped $BaCo_xZr_xFe_{(12-2x)}O_{19}$ prepared under sol–gel and citrate precursor sol–gel conditions. J Alloy Compd 2014;615:875–81.
[22] Chawla SK, Mudsainiyan RK, Meena SS, Yusuf SM. Sol–gel synthesis, structural and magnetic properties of nanoscale M-type barium hexaferrites $BaCo_xZr_xFe_{(12-2x)}O_{19}$. J Magn Magn Mater 2014;350:23–9.
[23] Fang Q, Bao H, Fang D, Wang J. Temperature dependence of magnetic properties of zinc and niobium doped strontium hexaferrite nanoparticles. J Appl Phys 2004;95:6360–3.
[24] Almessiere MA, Slimani Y, Güner S, van Leusen J, Baykal A, Kögerler P. Effect of Nb^{3+} ion substitution on the magnetic properties of $SrFe_{12}O_{19}$ hexaferrites. J Mater Sci: Mater Electron 2019;30:11181–92.
[25] Kanagesan S, Hashim M, Jesurani S, Kalaivani T, Ismail I. Microwave sintering of Zn-Nb doped barium hexaferrite synthesized via sol-gel method. Mater Sci Appl 2014;5:171.
[26] Almessiere MA, Slimani Y, Tashkandi N, Baykal A, Saraç MF, Trukhanov AV, et al. The effect of Nb substitution on magnetic properties of $BaFe_{12}O_{19}$ nanohexaferrites. Ceram Int 2019;45:1691–7.
[27] Silambarasu A, Manikandan A, Balakrishnan K. Room-temperature superparamagnetism and enhanced photocatalytic activity of magnetically reusable spinel $ZnFe_2O_4$ nanocatalysts. J Supercond Nov Magn 2017;30:2631–40.
[28] Maria Lumina Sonia M, Anand S, Maria-Vinosel V, Asisi Janifer M, Pauline S, Manikandan A. Effect of lattice strain on structure, morphology and magneto-dielectric properties of spinel $NiGd_xFe_{2-x}O_4$ ferrite nano-crystallites synthesized by sol-gel route. J Magn Magn Mater 2018;466:238–51.
[29] Maria-Lumina-Sonia M, Anand S, Blessi S, Pauline S, Manikandan A. Effect of surfactants (PVB/EDTA/CTAB) assisted sol-gel synthesis on structural, magnetic and dielectric properties of $NiFe_2O_4$ nanoparticles. Ceram Int 2018;44:22068–79.
[30] Elayakumar K, Manikandan A, Dinesh A, Thanrasu K, Kanmani Raja K, Thilak Kumar R, et al. Enhanced magnetic property and antibacterial biomedical activity of Ce^{3+} doped $CuFe_2O_4$ spinel nanoparticles synthesized by sol-gel method. J Magn Magn Mater 2019;478:140–7.
[31] Mallick KK, Shepherd P, Green RJ. Dielectric properties of M type barium hexaferrites prepared by co-precipitation. J Eur Ceram Soc 2007;27:2045–52.
[32] Slimani Y, Unal B, Hannachi E, Selmi A, Almessiere MA, Nawaz M, et al. Frequency and dc bias voltage dependent dielectric properties and electrical conductivity of $BaTiO_3$-$SrTiO_3$/$(SiO_2)_x$ nanocomposites. Ceram Int 2019;45:11989–2000.
[33] Unal B, Durmus Z, Kavas H, Baykal A, Toprak MS. Synthesis, conductivity and dielectric characterization of salicylic acid- Fe_3O_4 nanocomposite. Mater Chem Phys 2010;123:184.
[34] Ünal B, Baykal A. Effect of Zn substitution on electrical properties of nanocrystalline cobalt ferrite. J Supercond Nov Magn 2014;27:469.
[35] Auwal I, Ünal B, Baykal A, Kurtan U, Md Amir A, Yıldız Murat Sertkol. Electrical and dielectric properties of Y^{3+}-substituted barium hexaferrites. J Supercond Nov Magn 2017;30:1813–26.
[36] Pereira FMM, Santos MRP, Sohn RSTM, Almeida JS, Medeiros AML, Costa MM, et al. Magnetic and dielectric properties of the M-type barium strontium hexaferrite ($Ba_xSr_{1-x}Fe_{12}O_{19}$) in the RF and microwave (MW) frequency range. J Mater Sci: Mater Electron 2008;20:408.
[37] Honegger T, Berton K, Picard E, Peyrade D. Determination of Clausius-Mossotti factors and surface capacitances for colloidal particles. Appl Phys Lett 2011;98.
[38] Meena RS, Bhattachrya S, Chatterjee R. Complex permittivity, permeability and wideband microwave absorbing property of La^{3+} substituted U-type hexaferrite. J Magn Magn Mater 2010;322:1923.
[39] Wang S, Zhang C, Guo R, Liu L, Yang Y, Li K. Preparation and properties of yttria doped tetragonal zirconia polycrystal/Sr-doped barium hexaferrite ceramic composites. Mater Sci Eng, B 2015;193:91.
[40] Sözeri H, Baykal A, Ünal B. Low temperature synthesis of single domain Sr-hexaferrite particles by solid state reaction route. Phys Status Solidi A 2012;209:2002.